Mass Transport in Nanoarray Monolithic Catalysts: An Experimental-Theory Study

Xingxu Lu[a,b], Wenxiang Tang[a,b], Meilin Li[c], Yanliu Dang[c], Norwyn Campbell[d], Zihao Li[a,b], Steven L. Suib[b,c], Pu-Xian Gao[a,b,*]

[a] Department of Materials Science and Engineering, University of Connecticut, Storrs, CT 06269, USA

[b] Institute of Materials Science, University of Connecticut, Storrs, CT 06269, USA

[c] Department of Chemistry, University of Connecticut, Storrs, CT 06269, USA

[d] Department of Chemical and Biomolecular Engineering, University of Connecticut, Storrs, Connecticut 06269, USA

[*]Email: puxian.gao@uconn.edu

Abstract

Reducing the mass transfer resistance globally of a catalyst is a key to enhancing the catalytic reaction kinetics and fully utilizing the catalyst activity. Despite the success in tailoring the external mass transfer in the widely studied washcoat monoliths, the internal mass transfer resistance is difficult to be reduced due to the requirement of increasing macroporosity while maintaining high specific surface area and mechanical stability. Therefore, nanostructured array-based monolithic catalysts (nanoarray catalysts) have been developed in the past decade as a promising class of structured catalysts that may complement or substitute washcoat catalysts. This work fundamentally elucidates the enhanced mass transport properties of the nanoarray monolithic catalysts by a combination of experimental measurements and theoretical modeling. Using a low-dimensional model, the relative contributions of resistances were quantified in terms of chemical kinetics, internal and external mass transfers based on a probe model of C_2H_4 oxidation over the TiO_2 supported Pt-based monolithic catalysts. The nanoarray catalysts displayed a lower internal mass transfer resistance than the washcoat counterparts as a result of the high macroporosity and small thickness of nanoarray layers. The nanoarray configuration provides a new pathway towards designing high-performance monolithic reactors and catalysts with low internal diffusion limitations for various gas phase reactions.

KEYWORDS: Monolithic reactor; Nanoarray; Washcoat; Catalytic ethylene oxidation; Mass transfer.

1. Introduction

Since the first invention in 1960s, monolithic reactors have been widely used in the aftertreatment of automotive exhaust, catalytic oxidation of volatile organic compounds (VOCs), reducing pollutants from stationary emissions, and lately small molecular chemical and fuel processing [1-4]. Compared with packed-bed reactors, honeycomb monolith based structured reactors show advantages in terms of high heat and mass transport rates per unit pressure drop, small transverse temperature gradients, high throughput in reactions, and ease of scale-up for reactions and manufacturing [5]. The typical monolithic reactors, such as automotive catalytic converters, consist of parallel square channels (with a hydraulic diameter about 1 mm) with the catalytically active components loaded in the form of washcoat onto the surfaces of channel walls [6]. In commercial automotive catalytic converters, the washcoat layer of 40~200 μm in thickness is usually composed of mesoporous metal oxide supports such as γ-Al_2O_3 with high specific surface area, CeO_2-ZrO_2 for promoting oxygen storage and thermal stability as well as surface binding to improve the mechanical robustness [7]. Nanoparticles of platinum group metals (PGMs, such as Pt, Pd and Rh) are dispersed on mesoporous metal oxides as catalytically active components to catalyze the reactions within the monolithic channels [8].

In a washcoat based monolithic catalyst, the reaction of the gaseous reactants in the channels of a monolithic catalyst includes three major steps [7]: (i) the reactant diffusion from bulk gas phase stream to the top surface of the catalyst layer (washcoat), which is referred as external mass transfer; (ii) the reactant diffusion

within the catalyst layer to the catalytically active sites, which is noted as internal mass diffusion; (iii) chemical reactions on the surface of the catalytically active sites, which usually consist of adsorption, reaction and desorption processes. As illustrated in **Scheme 1**, the mass transport properties play important roles in the overall performance of washcoat monolithic catalysts.

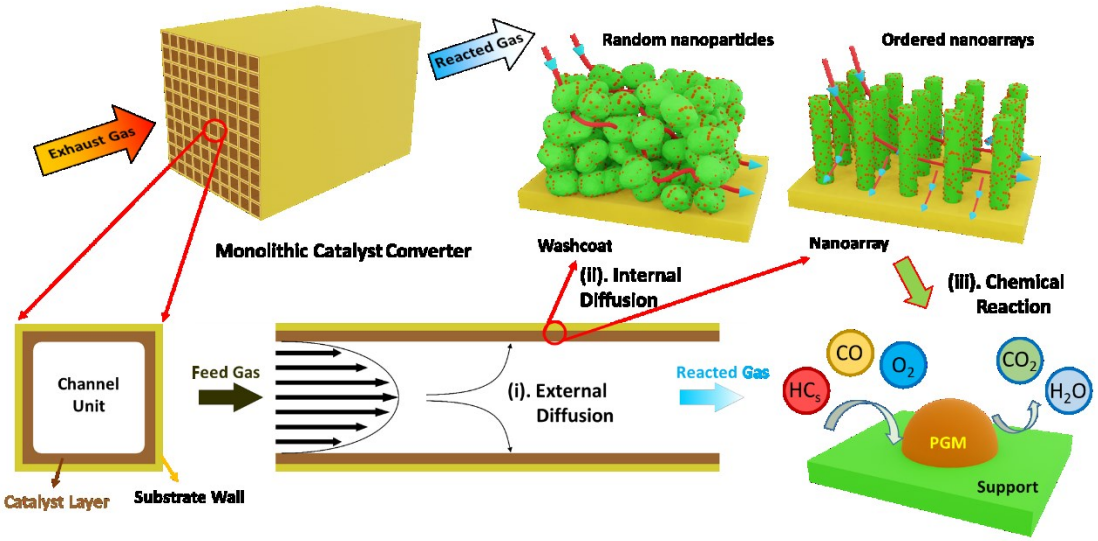

Scheme 1. Schematic diagram of a monolithic catalyst reactor, a representative channel, and the flow chart indicating the three major steps during the reaction in a monolith channel: (i) external diffusion, (ii) internal diffusion and (iii) chemical reaction.

The conversion efficiency of a monolithic catalyst is bounded by a three-fold resistance contributed by kinetic resistance at low temperature, internal mass transfer resistance at intermediate temperature, and external mass transfer resistance at high temperature [9]. Specifically, the kinetic resistance depends on the catalytic activity of the catalysts, which can be reduced by developing highly active catalysts. The

external mass transfer resistance depends on the geometric properties of the monolithic substrates and can be mitigated by optimizing the design of substrates [10, 11]. However, the internal mass transfer resistance is hard to be reduced due to dependence on both the effective diffusivity of the reactants within the washcoat layer and the washcoat thickness [12]. The washcoat is a complex porous network consisting of both mesopores (2~50 nm) and macropores (> 50 nm). The mesopores provide high specific surface area, which is important for the dispersion of catalytically active sites, but also result in strong internal mass transfer resistance, as shown in **Scheme1 (ii)**. The macropores, on the other hand, could enhance the internal mass transfer efficiency but decrease the specific surface area and mechanical stability of the catalysts. Therefore, the co-existence of both mesopores and macropores in the washcoat monolithic catalysts is indispensable and depends on various trade-offs [13, 14].

In order to step out from this dilemma and meet the challenges with a new perspective, a well-defined nanostructure array (nanoarray)-integrated structured catalyst configuration was invented and developed in the past decade and has been proven to be a promising class of cost-effective and efficient devices that may complement or substitute the washcoat catalysts [15-17]. Through facile hydrothermal methods, a wide spectrum of metal oxide nanoarrays, such as ZnO [18], TiO_2 [19, 20], CeO_2 [21], Co_3O_4 [22, 23], MnO_2 [24], and perovskite-type materials [25-27], have been successfully integrated onto the channel surfaces of the commercial cordierite honeycomb monolith. These ordered metal oxide nanoarrays can be employed either

as active catalysts for catalytic reactions or as the support material for other catalytically active components. Compared with the conventional particulate washcoat monolithic catalysts, nanoarray monolithic catalysts were demonstrated with enhanced materials utilization efficiency, improved thermal stability and mechanical robustness as well as tunable catalytic performance due to the well-defined structures [28, 29]. These merit features have been successfully proven by comparing the performance of the nanoarray monolithic catalysts and the washcoat counterparts directly in our previous studies [30-32]. For example, the excellent hydrothermal stability and sulfur poisoning resistance performance were demonstrated over the Pt/TiO_2 nanoarray-based monolithic catalysts following USDRIVE's testing protocol [30, 33]. Meanwhile, nanoarray catalysts show enhanced mass transport properties compared with washcoat catalysts [34]. As illustrated in **Scheme1 (ii)**, the ordered interspace between the uniform array units can help to facilitate the mass transfer of the reactant molecules between the nanoarrays, which better expose the active sites and promote gas–solid interaction by a much shorter diffusion length [15, 28]. Efforts have been made to demonstrate enhanced internal mass transport properties of the nanoarray monolithic catalysts. For example, Tang *et al.* [21] calculated the Weisz–Prater criterion number ($N_{W\text{-}P}$) of the Ceria nanoflake array supported Pt-based monolithic catalysts to be 0.023, which is much lower than the value of the washcoat catalysts ($N_{W\text{-}P}$ = 14.77). This indicates a much smaller internal mass transfer resistance in the nanoarray catalysts than the washcoat samples. Even though, direct experimental evidence and theoretical explanations are still

needed to elucidate the difference in the mass transport properties between the nanoarray and washcoat monolithic catalysts.

Meanwhile, a low-dimensional model was developed by Joshi. *et al.* [9, 10, 35] by averaging the governing equations and using the concepts of internal and external mass transfer coefficients. Based on the kinetics of the reactions, the diffusion properties of the washcoats and the geometric parameters of the monolithic catalysts, the resistance from the kinetic reactions, internal mass transfer and external mass transfer can be quantified as functions of various catalyst parameters and operating conditions [36]. This provides a chance to make quantitative comparisons between the nanoarray and the washcoat monolithic catalysts in terms of mass transport properties.

Therefore, this work is aimed to provide direct experimental evidence and theoretical explanations for the enhanced mass transport properties in the nanoarray monolithic catalysts over the washcoat counterparts. The oxidation of C_2H_4 was employed as a probe reaction, and a series of TiO_2 nanoarray and washcoat supported Pt-based monolithic catalysts were prepared and tested under different reaction conditions. Based on the experimental results, the relative contributions of resistances from chemical kinetics, internal mass transfer and external mass transfer were quantified as functions of various catalyst design and operating parameters using the low-dimensional model. Finally, the enhanced mass transport properties of the nanoarray catalyst were explained based on the influence of different parameters on the mass transfer resistance of both types of catalysts.

2. Experimental Procedures

2.1. Catalyst Preparation

The rutile TiO_2 nanoarrays were integrated onto the commercial cordierite monolithic honeycombs *via* a facile solvothermal method reported in our previous work [37]. In order to facilitate the heterogeneous growth of TiO_2 nanoarrays, the as-cleaned cordierite monoliths were firstly seeded with a TiO_2 polymeric sol (0.025 M), followed by annealing at 500 °C for 5 h to enhance the crystallinity of the seeds. In a typical synthesis process, 500 mL 2-butanone (C_4H_8O, 99+%, ACROS Organics™) was firstly added to a Teflon-lined autoclave as the organic solvent; then 50 mL hydrochloric acid (HCl, 37 wt.%, SIGMA-ALDRICH), 60 mL titanium (IV) *n*-butoxide (TBOT, 99%, ACROS Organics™), and 5 mL Titanium (IV) chloride ($TiCl_4$, 1M solution in Toluene, ACROS Organics™) were added in order and the mixture was stirred for 1 min. The seeded honeycomb (7cm×7cm×2.53cm) were soaked into the mixture solution slowly with the channels perpendicular to the bottom of the reactor. The autoclave reactor was then sealed and heated up to 150 °C and kept for 10 h in an electric oven. When the reaction was complete, the autoclave was cooled down in air, and the samples were rinsed with copious amount of water and ethanol under sonication. To ensure the removal of Cl^- ions, the DI water from the last cleaning cycle was tested with 1M $AgNO_3$ aqueous solution, and no white precipitate formed indicates the successful removal of Cl^- ions [38]. The samples were finally dried in an electric oven at 110 °C overnight.

Two types of Pt/TiO_2 nanoarray monolithic catalysts with loading ratios of 10 and 50 g-Pt/ft^3 were prepared and marked as NA-10 and NA-50, respectively. Pt nanoparticles (NPs) were deposited onto the TiO_2 nanoarray rooted monoliths through a microwave-assisted dip-coating process [34]. First, Tetraammineplatinum (II) nitrate ($Pt(NH_3)_4(NO_3)_2$, 99.99%, Alfa Aesar™) aqueous solution with a concentration of 1 mg-Pt/mL was prepared. Then proper amounts of $Pt(NH_3)_4(NO_3)_2$ aqueous solution were transferred into a 20 mL vial, and one piece of honeycomb (2.53 cm × 1 cm × 1 cm) was soaked into the solution under sonication. The liquid in the monolith channels was then blown back into the vial with an air gun before the sample was transferred to a domestic microwave oven with the channels in the horizontal direction and dried under microwave irradiation. After the samples became completely dry (microwave for 1~2 min), they were further dried at 250 °C for 10 min in an electric oven before the next dip-coating process. This deposition process was repeated for several cycles until all the solution in the vial was consumed. Finally, the dip-coated samples were calcined in oven at 500 °C for 5 h with a ramping rate of 2 °C/min.

The washcoat Pt-based monolithic catalysts were prepared with the same amount of Pt loading of 10 and 50 g-Pt/ft^3 as the nanoarray catalysts and marked as WC-10 and WC-50, respectively. Two types of TiO_2 NPs supported Pt-based catalysts containing 0.1 and 0.5 wt. % Pt were prepared via wet impregnation methods [39]. Firstly, a slurry consisting of 10 g pre-calcined P25 TiO_2 and 200 mL DI water was maintained at 80 °C under stirring, and nitric acid was added drop-wise to reach a stable pH of 4.

Then the desired amount of the $Pt(NH_3)_4(NO_3)_2$ aqueous solution (1 mg-Pt/mL) was added drop-wise into the slurry under stirring. After 2 h under stirring, the slurry was transferred to an electric oven with caps on and kept at 80 ºC for 12 h, and then the solution was evaporated in open air at 80 °C under stirring until dry. Finally, the collected catalyst powders were calcined in oven at 500 °C for 2 h with a ramping rate of 2 °C/min. The washcoat monolithic catalysts were prepared by dipping a pre-calcined cordierite honeycomb substrate into a catalyst powder suspension. The catalyst powder was mixed with a binder (γ-Al_2O_3, Alfa Aesar™, catalyst/binder = 4/1 in weight) and dispersed in a solution made of 50 wt.% ethanol and 50 wt.% water. The liquid-to-solid mass ratio of the slurry was around 5 to ensure the deposition of a sufficient amount of washcoat and avoid channel clogging. After each dipping, the liquid phase in the monolith channels was blown back into the vial with an air gun, and the samples were dried at 300 °C for ten minutes. The dipping and drying process was repeated until a desired amount of washcoat was deposited. Finally, the monoliths were calcined in oven at 500 °C for 5 h with a ramping rate of 2 °C/min.

Before the catalytic performance tests, all the catalysts were pre-oxidized in a flow of 10% [O_2] in N_2 at 500 °C for 1 hour to remove any contaminant, followed by a reduction treatment in an atmosphere of 10% [H_2] in N_2 at 300 °C for 1 hour. Finally, all the samples were degreened in a gas flow of 1000 ppm [C_2H_4] + 5% [O_2] balanced by N_2 at 700 °C for 4 hours.

2.2. Catalyst Characterization

The morphology and microstructure of the nanoarray and washcoat catalysts were characterized by a Field-emission Scanning Electron Microscope (SEM, ThermoFisher TeneoLoVac) [40] and a Scanning/Transmission Electron Microscope (TEM/STEM, ThermoFisher Titan Themis). The surface areas were calculated by the Brunauer–Emmett–Teller (BET) method from the nitrogen adsorption–desorption isotherms measured at 77 K using a Quantochrome Autosorb iQ2 automated gas sorption analyzer [41]. The porosity were obtained with the Barrett, Joyner, and Halenda (BJH) method using the desorption branch of the isotherm. The samples for BET analysis include both the nanoarrays/washcoat and the cordierite substrate. Prior to the analyses, the samples were degassed at 150 °C for 4 h to remove any adsorbed species.

2.3. Catalyst Performance Evaluation

The catalytic performances of the samples were evaluated using a fixed-bed quartz reactor [42] connected with an online FTIR (ThermoFisher Nicolet 6700) equipped with a 2 m path-length gas cell (250 mL volume). In order to study the reaction kinetics of C_2H_4 oxidation over the catalysts, C_2H_4 with different concentrations were added into the feed gas with excess O_2 (1%). The inlet concentrations of C_2H_4 were kept low (<1000 ppm) to maintain isothermal conditions at low conversions. The total flow rates were kept at 500 sccm for all tests, and the space velocity can be adjusted

by changing the number of channels for the monoliths. Detailed parameters for the tests are summarized in **Table S1.**

The oxidation reactions were carried out in a temperature range of 60-500 °C with a ramping rate of 2 °C/min. A thermocouple was inserted into the reactor for measuring the catalyst inlet temperature, and the exit conversion (η) of C_2H_4 was monitored by an online FTIR using the following equation:

$$\eta = \frac{C_{in} - C_{out}}{C_{in}} \times 100\% \quad (1)$$

3. Theoretical Modelling

In order to quantify the relative contribution of resistances from chemical kinetics, internal mass transfer and external mass transfer, respectively, a low-dimensional model for single washcoat monolith channel was adopted following the work of Joshi *et al.* [35]. The low dimension formulation is accomplished by averaging the convection-diffusion-reaction equations in the transverse direction which leads to an approximation of transverse diffusion and reaction with an overall mass transfer coefficient [35, 43, 44]. Key assumptions justified in this prior work include: (a) laminar flow in the monolith channel, as indicated in **Scheme 1**; (b) negligible fluid phase axial diffusion and heat conduction in the fluid phase compared to convection; (c) constant physical properties [9, 10]. The low-dimensional model consists of transport equations accounting for the species mass balances in the (i) gas fluid phase, (ii) washcoat phase and (iii) gas-solid interface as follows [36]:

(i). Gas fluid phase species balance:

$$\frac{\partial C_f}{\partial t} = -\langle u \rangle \frac{\partial C_f}{\partial z} - \frac{1}{R_{\Omega 1}} k_{me} \left(C_f - C_s \right) \tag{2}$$

(ii). Washcoat phase species balance:

$$\varepsilon_{wc} R_{\Omega 2} \frac{\partial \langle C_{wc} \rangle}{\partial t} = k_{mi} \left(C_s - \langle C_{wc} \rangle \right) - R_{\Omega 2} R\left(\langle C_{wc} \rangle \right) \tag{3}$$

(iii). Gas-solid interface species balance:

$$k_{me} \left(C_f - C_s \right) = k_{mi} \left(C_s - \langle C_{wc} \rangle \right) \tag{4}$$

Boundary inlet conditions:

$$C_f = C_{in} \ @ \ z = 0 \tag{5}$$

Here C_f, C_s and $\langle C_{wc} \rangle$ are the average mole fractions of C_2H_4 in the fluid, gas-solid interface and washcoat phase, respectively. $\langle u \rangle$ is the average fluid velocity and ε_{wc} is the washcoat porosity. R_{Ω_1} and R_{Ω_2} are the effective transverse diffusion lengths for the fluid and washcoat phases, respectively, which can be determined according to the geometry features of the monolith and washcoat layers [10]. $R\left(\langle C_{wc} \rangle \right)$ is the reaction rate in the washcoat. k_{me} and k_{mi} are the external and internal mass-transfer coefficients given by:

$$k_{me}(z) = Sh_e(z) \frac{D_f}{4R_{\Omega_1}} \quad , \quad k_{mi}(z) = Sh_i(z) \frac{D_e}{R_{\Omega_2}} \tag{6}$$

where D_f is the temperature-dependent molecular diffusivity of reactant in the fluid phase, which can be estimated using the Lennard-Jones potentials [45], and D_e is the

effective diffusivity of the reactant in the washcoat phase. The parameter D_e can be related to D_f as follows:

$$\mu = D_f / D_e \tag{7}$$

The reported value of μ ranges from 10 to 100 according to the features of washcoat layers [13, 46-48], and was assumed to be 30 for the washcoat catalysts in this work according to the reported measurements [49, 50]. The value of μ was assumed to be 1 for the nanoarray catalysts during the modeling in this work according to the proposed enhancement in internal mass transport efficiency. However, the value of μ has no significant influence on the conversion efficiency of the nanoarray catalysts, which will be discussed in detail in **Section 4.5.** Sh_e and Sh_i represent the dimensionless external and internal Sherwood numbers, respectively. The external Sherwood number Sh_e for the fully developed flow in a channel is given by [11, 51]:

$$Sh_e = Sh_{H2,\infty} + \frac{0.108\left(f\,\mathrm{Re}\right)_\infty^{1/3}\left(\frac{P}{z}\right)}{1+0.083\left(\frac{P}{z}\right)^{2/3}} \tag{8}$$

where $Sh_{H2,\infty}$ and $(f\,\mathrm{Re})_\infty$ are the asymptotic values of Sherwood number and friction factor times Reynolds number for fully developed flow, respectively. Their values depend on the geometric shapes of the channels [11]. z is the dimensionless length and P is the transverse mass Peclet number, which is defined by:

$$P = \frac{\langle u \rangle R_{\Omega_1}{}^2}{D_f L} \tag{9}$$

The internal Sherwood number Sh_i can be calculated using the expression [10]:

$$Sh_i = Sh_{i,\infty} + \frac{\Lambda\phi^2}{1+\Lambda\phi} \tag{10}$$

where the parameters $Sh_{i,\infty}$ and the constant Λ depends only on the geometric shape of the washcoat [10]. ϕ is the Thiele modulus, which is used to describe the relationship between diffusion and reaction rate in the washcoat catalyst. ϕ can be calculated using the following equation [10]:

$$\phi^2 = \frac{R\left(\langle C_{wc}\rangle\right)\left(R_{\Omega_2}\right)^2}{\langle C_{wc}\rangle D_e} \tag{11}$$

where $R\left(\langle C_{wc}\rangle\right)$ is the reaction rate in the washcoat. In the case of first-order kinetics, $R\left(\langle C_{wc}\rangle\right) = k\langle C_{wc}\rangle$, where k is the first-order reaction rate constant, so **Eq. 11** can be simplified as:

$$\phi^2 = \left(R_{\Omega_2}\right)^2 \frac{k}{D_e} \tag{12}$$

With all these parameters, the individual resistance from the chemical kinetics, internal mass transfer and external mass transfer can be defined as follows:

(i) External mass transfer resistance:

$$R_{ex} = \frac{1}{k_{me}} = \frac{4R_{\Omega_1}}{Sh_e D_f} \tag{13}$$

(ii) Internal mass transfer resistance:

$$R_{in} = \frac{1}{k_{mi}} = \frac{R_{\Omega_2}}{Sh_i D_e} \tag{14}$$

(iii) Kinetic resistance:

$$R_{re} = \frac{\langle C_{wc} \rangle}{R_{\Omega_2} R\left(\langle C_{wc} \rangle\right)} \tag{15}$$

Therefore, the total resistance can be calculated as:

$$R_t = \frac{1}{k_{mapp}} = \frac{1}{k_{me}} + \frac{1}{k_{mi}} + \frac{\langle C_{wc} \rangle}{R_{\Omega_2} R\left(\langle C_{wc} \rangle\right)} = \frac{4R_{\Omega_1}}{Sh_e D_f} + \frac{R_{\Omega_2}}{Sh_i D_e} + \frac{\langle C_{wc} \rangle}{R_{\Omega_2} R\left(\langle C_{wc} \rangle\right)} \tag{16}$$

where k_{mapp} is the apparent mass transfer coefficient. For a working catalytic monolith, the governing equation at steady state can be expressed using the experimentally observable apparent mass transfer coefficient k_{mapp} as:

$$\langle u \rangle \frac{dC_f}{dz} = -\frac{k_{mapp}(z)}{R_{\Omega 1}} C_f, \; C_f = \alpha_1 C_{in} \;\; @ \; z = 0 \tag{17}$$

where α_1 is the first normalized Fourier weight depending on the channel geometry and is between 0.8 and 1.0. Integrating the above equation:

$$C_f = \alpha_1 C_{in} \exp\left(-\frac{k_{mapp}}{\langle u \rangle R_{\Omega 1}} z \right) \tag{18}$$

Make $z = L$, the reactant concentration at the exit:

$$C_{exit} = \alpha_1 C_{in} \exp\left(-\frac{k_{mapp}}{\langle u \rangle R_{\Omega 1}} L \right) \tag{19}$$

Thus, the simulated exit conversion is related to the monolith temperature as follows:

$$\chi = 1 - \frac{C_{exit}}{C_{in}} = 1 - \alpha_1 \exp\left(-\frac{k_{mapp}}{\langle u \rangle R_{\Omega 1}} L \right) \tag{20}$$

The specific parameters for the nanoarray and washcoat monolithic catalysts tested in this work are summarized in **Table 1**.

4. Results and Discussion

4.1. Catalyst Microstructure and Physicochemical Properties

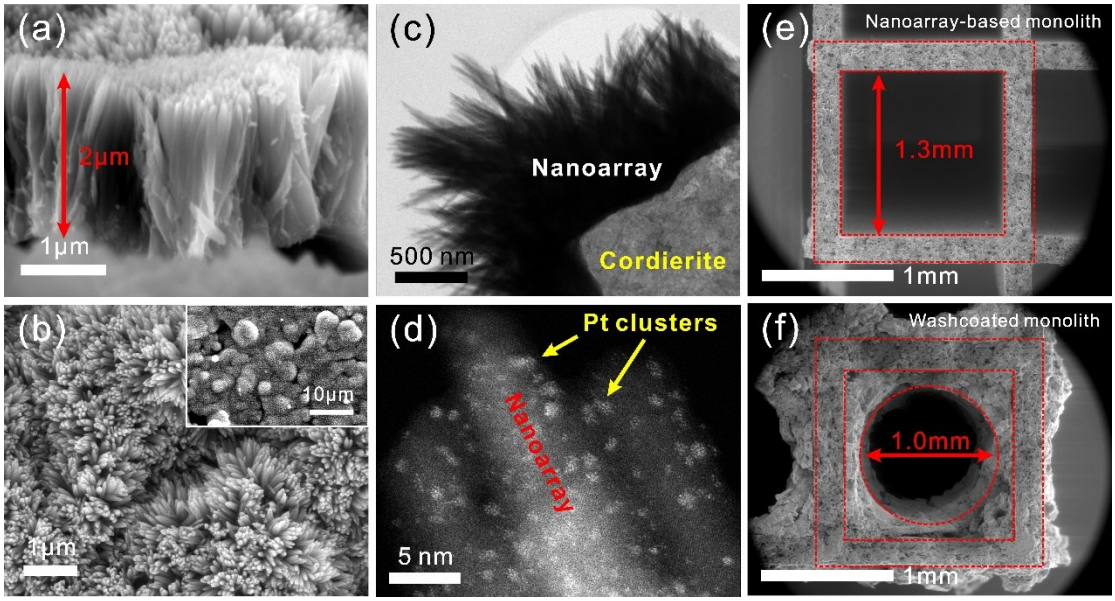

Figure 1. Morphology and microstructure of the TiO_2 nanoarray integrated monoliths: SEM images of the (a) cross-sectional view and (b) top view of the TiO_2 nanoarrays; (c) BF and (d) HAADF images of the TiO_2 nanoarray supported Pt catalysts. SEM images of the front view of channel structure and its geometric features of the (e) nanoarray based and (f) washcoat monoliths.

The SEM images in **Figure 1 (a)** and **(b)** display the cross-sectional view and top view of the TiO_2 nanoarray integrated monolithic honeycomb, respectively. The nanoarrays are composed of vertically aligned nanorods with an average length of ~2 μm and a diameter of 50-100 nm. Higher magnified bright field (BF) TEM images in

Figure 1(c) reveal that the individual nanorods consists of a bundle of thinner nanowires with an average diameter of ~10 nm, which agrees well with our previous research [30, 37]. The interface between the nanoarrays and the substrate surfaces shown in the TEM images can withstand sonication in water for 4 hours, which establishes the good mechanical stability of the final catalyst [34, 52]. The high angle annular dark field (HAADF) image of the TiO_2 nanoarray supported Pt catalysts shown in **Figure 1 (d)** reveals that uniform sub-nano Pt clusters are decorated onto the TiO_2 nanowires. The highly dispersed Pt nano clusters provide abundant active sites that promote the catalytic reactions [42]. Meanwhile, the ordered interspace between the array units in **Figure 1 (b)** makes the catalytically active sites directly exposed in the reactant gas flow, which greatly enhances the internal diffusion efficiency of the reactant molecules between the nanoarrays compared to the diffusion in the washcoats, as was illustrated in **Scheme 1 (ii)** [21]. The promoting effects of the ordered nanoarray structure on the internal mass transport efficiency will be discussed in detail in **Section 4.5**. **Figures 1 (e)** and **(f)** reveal the geometries of the monolith channels and washcoat layers, respectively. The side length of the inner channels of the honeycomb is ~1.3 mm. If a round shape of the cross section of the washcoat channel is assumed, as shown in **Figure 1(f)**, the average radius of the washcoat channels was measured to be 0.533 and 0.522 mm for the washcoat catalysts WC-50 and WC-10, respectively. Therefore, the effective transverse diffusion length for the fluid phase (R_{Ω_1}) and washcoat phase (R_{Ω_2}) can be determined [10]. For the nanoarray based catalysts, since the average length of the nanoarrays is

negligible compared to the size of the monolith channels, the value of $R_{\Omega 2}$ for the nanoarray catalysts was assumed to be equal to the average thickness of the nanoarray layers, and the R_{Ω_1} can also be calculated accordingly. **Table 1** summarizes the physicochemical properties and geometrical parameters used for the low-dimensional model mass transport simulation.

Table 1. Physicochemical properties and geometrical parameters of monolithic catalysts used in the mass transport simulation.

Properties	WC-50	WC-10	NA-50	NA-10
Support type	Washcoat	Washcoat	Nanoarray	Nanoarray
Pt loading [g/ft^3]	50	10	50	10
S_{BET} [m^2/g_{cat}] [a]	17.5	15.9	8.5	7.5
R_{Ω_1} [μm]	262	261	323	323
R_{Ω_2} [μm]	262	238	2	2
$Sh_{i,\infty}$ [b]	2.533	2.533	2.645	2.645
Λ [b]	0.73	0.73	0.58	0.58
$Sh_{H2,\infty}$ [c]	4.364	4.364	3.089	3.089
$(f\,\mathrm{Re})_\infty$ [c]	16	16	14.32	14.32
μ	30	30	1	1

[a]: BET surface area, substrate included.

[b]: Parameters determined from the Ref. [10].

[c]: Parameters determined from the Ref. [11].

4.2. Catalyst Performance in Total Ethylene Oxidation

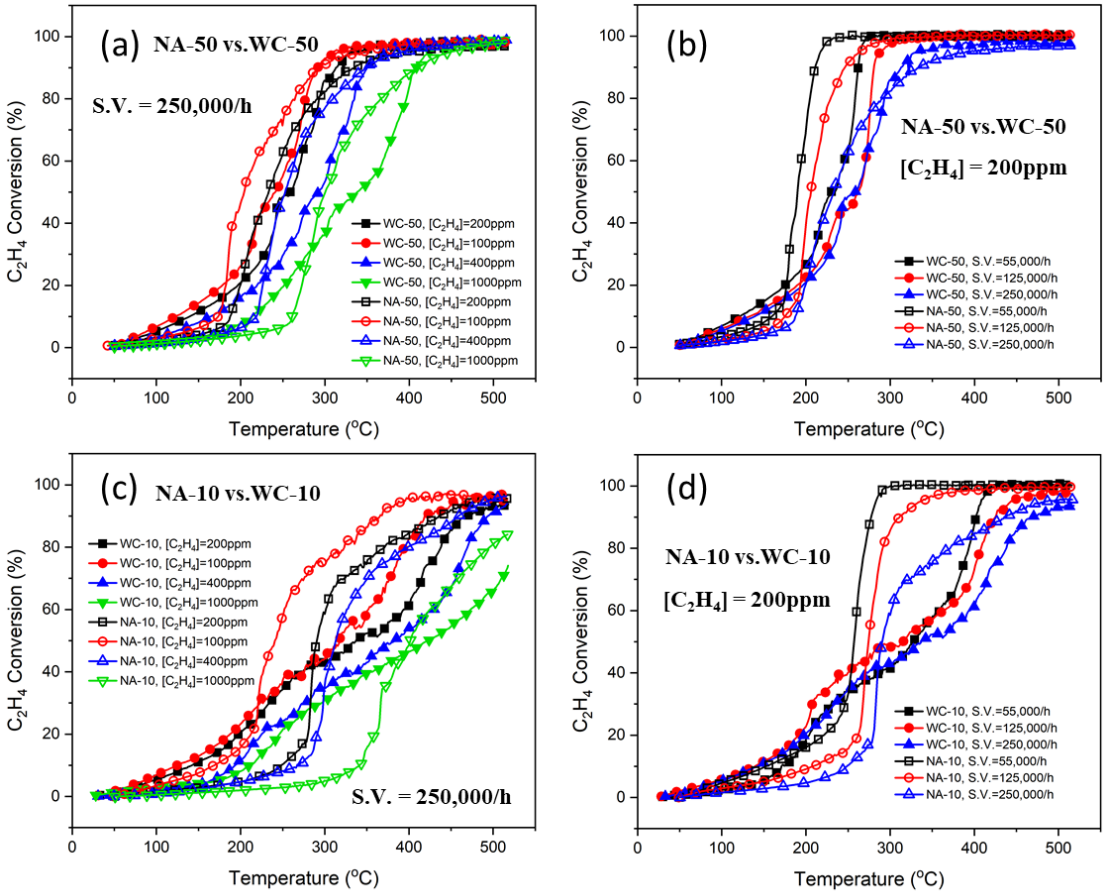

Figure 2. Exit C_2H_4 conversion as a function of the monolith temperature for the catalytic tests with different C_2H_4 feed concentrations and space velocities: (a) NA-50 vs WC-50 and (c) NA-10 vs WC-10 with S.V. = 250,000/h and different C_2H_4 feed concentrations; (b) NA-50 vs WC-50 and (d) NA-10 vs WC-10 with $[C_2H_4]$ = 200 ppm and different space velocities. Open symbol for nanoarray catalysts, close symbol for washcoat catalysts.

The light-off curves of C_2H_4 oxidation are displayed in **Figure 2** for the nanoarray monolithic catalysts (NA-10 and NA-50, open symbol) and washcoat monolithic catalysts (WC-10 and WC-50, solid symbol) under different conditions, including C_2H_4 feed concentration and space velocity. More detailed one-to-one comparison between the nanoarray catalysts and their corresponding washcoat counterparts can be found in **Figure S1**. Three interesting phenomena can be observed from these light-off curves: (i) the washcoat catalysts light off earlier than the nanoarray counterparts in the low-temperature range; (ii) the light-off curves of the nanoarray catalysts climb faster than that of the washcoat catalysts in the intermediate temperature range; (iii) for the catalysts loaded with 50g/ft^3 Pt (NA-50 and WC-50), the light-off curves of the nanoarray catalysts are slower to reach the conversion limits than the washcoat catalysts in the high temperature range when the space velocity is high (S.V. = 250,000/h).

The conversion efficiency of a monolithic catalyst is dictated by the reaction kinetics resistance at low temperatures, the internal mass transfer resistance at intermediate temperatures, and the external mass transfer resistance at high temperature, respectively [9]. At low temperatures, the kinetic reaction is the rate limiting step, when the reactants can be quickly consumed and refreshed through the external and internal mass transfer. Therefore, the observed early light-off of washcoat catalysts at low temperatures in **Figure 2** indicates that the washcoat catalysts have lower kinetic resistance than the nanoarray catalysts at low temperatures in the present work. The smaller kinetic barrier of the washcoat catalysts was also evidenced by the

lower activation energy of the washcoat catalysts ($\overline{E_a^{WC}} \approx 22.36\text{kJ/mol}$) than that of the nanoarray catalysts ($\overline{E_a^{NA}} \approx 37.10\text{kJ/mol}$), as presented in **Figure 3 (a)** and **(b)**. One possible reason for the different kinetic resistances may be that the washcoat monolithic catalysts have high specific surface area than the nanoarray counterparts, as displayed in **Table 1** and presented in **Figure S2**. The higher specific surface area can provide more catalytically active sites on the surface of the catalysts, and thus, result in a lower kinetic resistance at low temperatures. Meanwhile, since the internal diffusion is not the rate limiting step at low temperatures, the high surface area of the washcoat layer won't significantly increase the internal mass transfer resistance, and therefore, won't compromise the overall conversion efficiency at low temperatures.

The kinetic reaction rate increases rapidly with the operating temperature, and in most cases, the increase is exponential with temperature (Arrhenius dependence). On the other hand, the diffusivities of the reactant species in the gas phase and washcoat layers are weak functions of the operating temperature, and therefore the external and internal mass transfer resistance increase gradually with increasing temperature [9]. These could help to explain the second observation in **Figure 2** that the light-off curves of the nanoarray catalysts climb faster than the washcoat catalysts in the intermediate temperature ranges. As the monolith temperature increases, the reaction rate increases rapidly and the kinetic barrier becomes negligible very quickly. Meanwhile, the internal diffusion of the reactant species in the washcoat layers become the rate limiting step, and the internal mass transfer resistance imposes a dominant influence on the conversion efficiency of the monolithic catalysts in the

intermediate temperature ranges. The observation that light-off curves of the nanoarray catalysts climb faster indicates that the nanoarray monolithic catalysts have lower internal mass transfer resistance than the washcoat counterparts. This agrees well with the assumption that the ordered and macroporous channels between adjacent nanoarray units can result in better exposure of active sites and promotes gas–solid interaction by a much shorter diffusion length [15]. This is the focus of this work and will be discussed in detail with the aid of a low-dimensional model in the following sections. The third phenomenon that nanoarray catalysts are slower to reach the conversion limits in the case of high space velocity can be explained by the difference in the external mass transfer resistance caused by the different geometries of the nanoarray and the washcoat monolith, which will be addressed in **Section 4.6**.

4.3. Reaction Kinetics

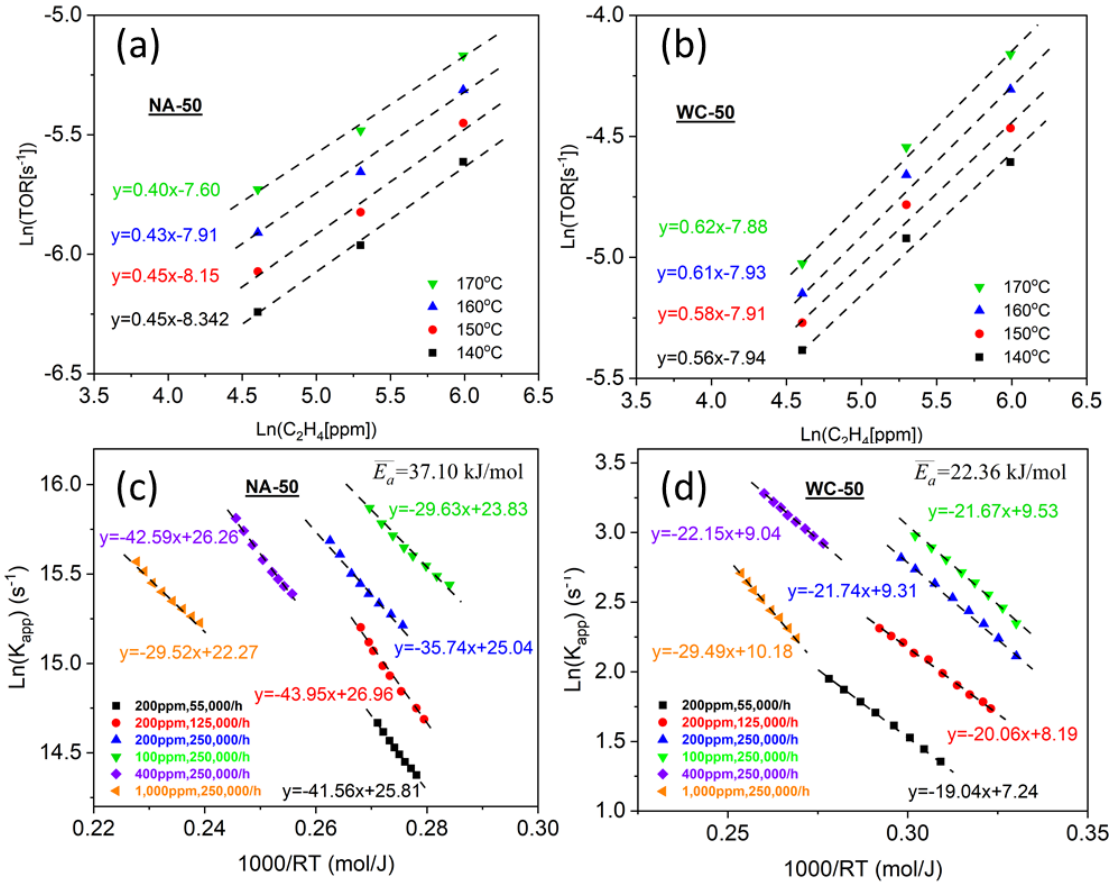

Figure 3. Determination of the kinetics for C_2H_4 oxidation over the NA-50 and WC-50 catalysts assuming a differential reactor: (a, b) effects of the initial C_2H_4 concentration on the TOR for C_2H_4 oxidation over the (a) nanoarray NA-50 and (b) washcoat WC-50 catalysts; (c, d) Arrhenius plots for C_2H_4 oxidation over the (c) nanoarray NA-50 and (d) washcoat WC-50 catalysts.

The experimental data below 15% conversion over the NA-50 and WC-50 catalysts were used to evaluate the reaction kinetics under different reaction conditions. The dependence of the reaction turnover rate (TOR) on C_2H_4 concentration was determined by establishing the gas feed conditions with excess O_2 (1%) and varying

the C_2H_4 concentrations (100, 200 and 400 ppm) under different temperatures. **Figures 3 (a)** and **(b)** display the effects of C_2H_4 concentration on the TOR for C_2H_4 oxidation over the NA-50 and WC-50 catalysts at low temperatures (140, 150, 160 and 170 °C). The rate is expressed as a TOR defined as moles of C_2H_4 reacted per mole of Pt per second, and the total moles of Pt were calculated using the loading ratio (50g/ft^3 Pt) and the volume of the monolith. The reaction order numbers over the NA-50 nanoarray catalyst and WC-50 washcoat catalysts are 0.43±0.03 and 0.59±0.03, respectively. On the other hand, the apparent activation energy of the catalysts under different conditions can be estimated by plotting the reaction rate constant as a function of temperature (Arrhenius plot). As shown in **Figures 3 (c)** and **(d)**, assuming first-order kinetics, TOR = $K_{app}C$, where C is the concentration of C_2H_4, and K_{app} is the apparent rate constant, the apparent activation energy of the NA-50 nanoarray catalysts at low temperatures is $\overline{E_a^{NA}} \approx 37.10$kJ/mol (**Figure 3 (a)**), while the value for the WC-50 washcoat catalysts is $\overline{E_a^{WC}} \approx 22.36$kJ/mol (**Figure 3 (b)**). According to the Arrhenius equation, a higher apparent activation energy would cause the reaction to be more sensitive to the reacting temperature [53]. In the present work, the higher apparent activation energy of the NA-50 nanoarray catalyst causes light off to occur later that the WC-50 washcoat catalysts in the low temperature ranges. However, as the temperature increases, the reaction rate over the NA-50 nanoarray catalyst increases more rapidly than the WC-50 washcoat catalysts due to the higher apparent activation energy, and therefore, the light-off curves of the nanoarray

catalysts climb faster than the washcoat catalysts in the intermediate temperature ranges.

Furthermore, when the internal diffusion limitation is significant for a catalytic reaction, the following relationships can be expected between the true reaction order number (n) and the apparent reaction order number (n') as well as the true activation energy (E_T) and the apparent activation energy (E_{app}) [12, 53]:

$$n' = \frac{1+n}{2} \tag{21}$$

$$E_T = 2E_{app} \tag{22}$$

The calculated apparent reaction order numbers and activation energies of the NA-50 nanoarray catalyst and the WC-50 washcoat catalyst agree very well with Eqs. (21) and (22). This implies that the activation energy of the nanoarray catalysts is closer to the true value, while the value of the washcoat catalysts deviates more from the true activation energy due to the existence of strong internal diffusion limitations. Therefore, this provides another strong evidence that nanoarray monolithic catalysts have lower internal mass transfer resistance than the washcoat catalysts for the reactions in this work.

The catalytic oxidation of C_2H_4 over the Pt catalysts has been extensively studied and was reported to follow a Langmuir-Hinshelwood (L-H) mechanism that the adsorbed ethylene molecule reacts with the dissociated oxygen atoms on the surface of Pt nanocrystallites [54, 55]. Meanwhile, Kua and Goddard [56] reported a lower binding energy for C_2H_4 than O_2 on the Pt(111) surface, so the noble-metal surface is

more easily covered by O_2. This agrees with the observation by Ackelid et. al. [54] that the surface is completely dominated by oxygen and that the coverage of ethylene-derived species is negligible when O_2 is in excess in the reaction atmosphere. Therefore, using the obtained apparent activation energy and reaction order number as the initial input, the experimental data were fitted over the entire temperature range using the low dimensional model by Joshi *et al.* [9, 10, 35, 57]:

$$\mathrm{TOR} = \frac{k_1 \langle C_{wc} \rangle}{\left(1 + k_2 \langle C_{wc} \rangle\right)^2} \tag{21}$$

$$k_1 = A_1 \cdot \exp\left(-\frac{\Delta E_1}{RT}\right) \tag{22}$$

$$k_2 = A_2 \cdot \exp\left(-\frac{\Delta E_2}{RT}\right) \tag{23}$$

TOR represents the reaction turn-over rate (mole of C_2H_4 reacted per unit volume of washcoat/nanoarray per second) with units of [mol/m^3 of washcoat or nanoarray/s], and $\langle C_{wc} \rangle$ are the averaged mole fraction of C_2H_4 in the washcoat/nanoarray phase. k_1 and k_2 are exponential parameters to be optimized with the experimental data. Using the power-law model as an initial guess, the following parameters for the washcoat and nanoarray catalysts are obtained and summarized in **Table 2**. Good agreement between the experimental data and the simulations is evident from **Figure 4**.

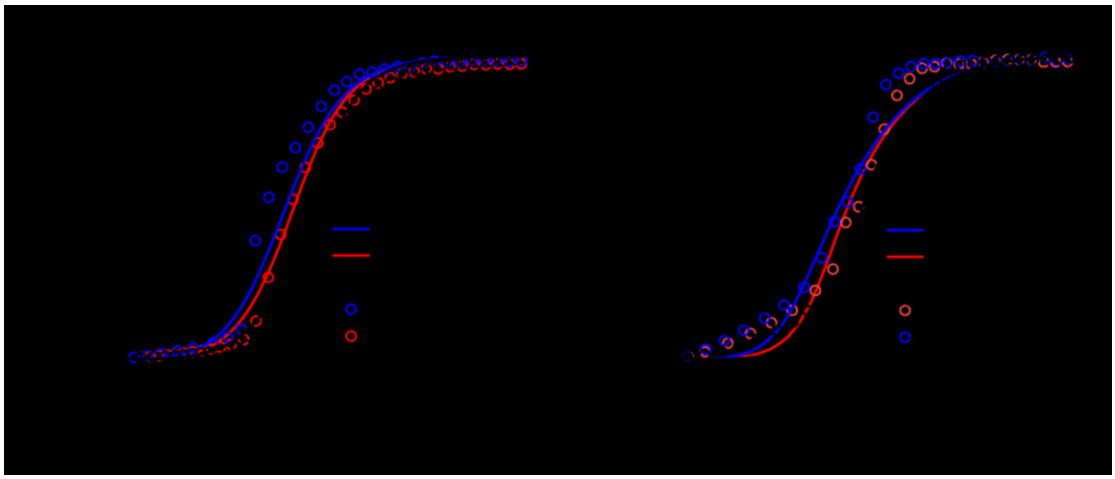

Figure 4. Exit C_2H_4 conversion as a function of the monolithic temperature for different C_2H_4 feed concentrations during C_2H_4 oxidation over the (a) NA-50 and (b) WC-50 catalysts. (curves: simulations using the LD model; markers: experimental data.)

Table 2. Optimized parameters for the L-H models of the washcoat and nanoarray catalysts.

Catalysts	A_1	ΔE_1	A_2	ΔE_2
NA-50	6.5×10^{8}	4.65×10^{4}	50	-150
WC-50	6.3×10^{8}	5.5×10^{4}	150	-150

4.4. Resistance Quantification

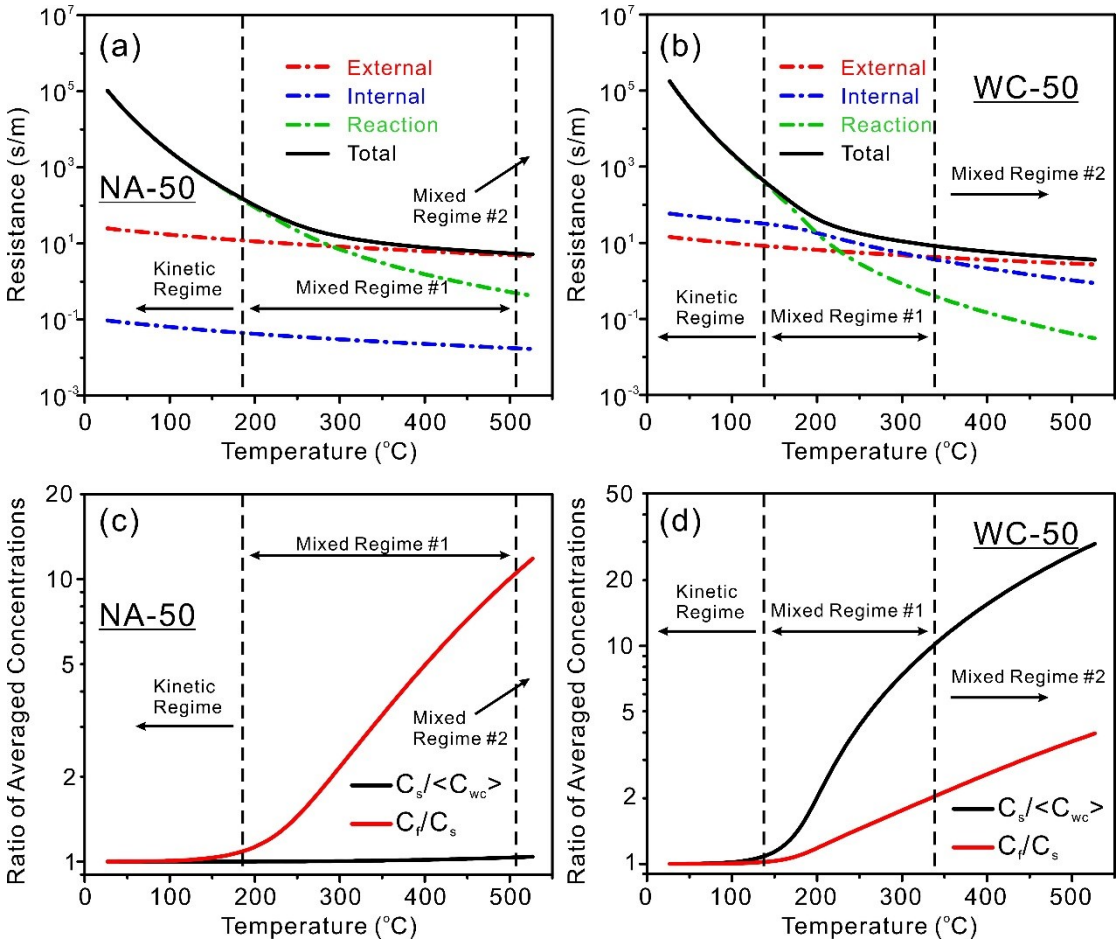

Figure 5. Calculated (a, b) resistance and (c, d) ratio of averaged concentrations as the function of the monolithic temperature over the (a, c) NA-50 and (b, d) WC-50 catalysts. Reaction conditions: C_{in} = 200 ppm C_2H_4, S.V. = 250,000/h.

In this sections, the relative contribution of resistances from chemical kinetics, internal mass transfer, and external mass transfer are quantified as a function of the monolith temperature using the low dimensional model [35]. Since the reaction resistance and internal mass transfer resistance are a function of the inlet concentration, the resistance along the monolith temperature also depends on the inlet concentration. Therefore, the reaction gas feed conditions 1-3 in **Table S1** (200 ppm

C_2H_4, S.V. = 250,000/h) were used to illustrate the difference in the resistance between the NA-50 and WC-50 catalysts. The other parameters were taken from **Table 1**. The controlling regimes were identified according to the criteria proposed by Joshi *et al.*[57, 58].

Each resistance is a monotonically decreasing function of the temperature for both catalysts. Particularly, the internal and external mass transfer resistance decrease smoothly because they are weak functions of temperature, while the kinetic resistance decreases sharply because the Arrhenius equations (**Eq. 21**-**23**) depend on the temperature. The most important observation from the **Figures 5 (a)** and **(b)** is that the internal mass transfer resistance in the NA-50 catalyst is much lower than that in the WC-50 catalyst. The kinetic resistance and external mass transfer resistance are always at least an order of magnitude higher than the internal mass transfer resistance in the NA-50 catalysts over the entire temperature range (**Figure 5a**). Therefore, the reaction transitions from the kinetic resistance controlling regime to the mixed controlling regime by kinetic and external mass transfer resistance at ~185 °C, and internal mass transfer resistance is negligible over the entire temperature range. On the other hand, for the WC-50 catalyst, the internal mass transfer resistance is on the same scale as the external mass transfer resistance (**Figure 5b**), and both of them decrease gradually with temperature. Therefore, as the temperature decreases, the kinetic resistance decreases sharply, and the reaction transitions from the kinetic resistance controlling regime to a mixed regime controlled by all three resistances in the temperature range of 150~350 °C. The internal mass transfer resistance plays a

significant role in this temperature range. This can explain why the light-off curves of the nanoarray catalysts climbs much faster than the washcoat catalysts in the intermediate temperature range in **Figure 2**.

The ratio of the different averaged concentrations is another indicator of the significance of different resistance components [9]. **Figure 5 (c)** and **(d)** present the ratio of average concentrations, C_f / C_s and $C_s / \langle C_{wc} \rangle$, at temperatures over the NA-50 and WC-50 catalysts. For the nanoarray catalysts, the value of $C_s / \langle C_{wc} \rangle$ remains close to 1 over the entire temperature range (black line), which indicates a small internal mass transfer barrier between the fluid-solid interface and the nanoarray phase. The value of C_f / C_s increases gradually with temperature, and the external mass transfer resistance becomes dominant with increasing temperature (red line). On the other hand, the evolution of the averaged concentration ratios is quite different in the WC-50 catalyst. As can be seen in **Figure 5 (d)**, the ratio of $C_s / \langle C_{wc} \rangle$ increases sharply with temperature, suggesting a significant internal mass transfer resistance during the reaction process. Such results agree with calculations of washcoat monolithic catalysts in the literature [9, 12].

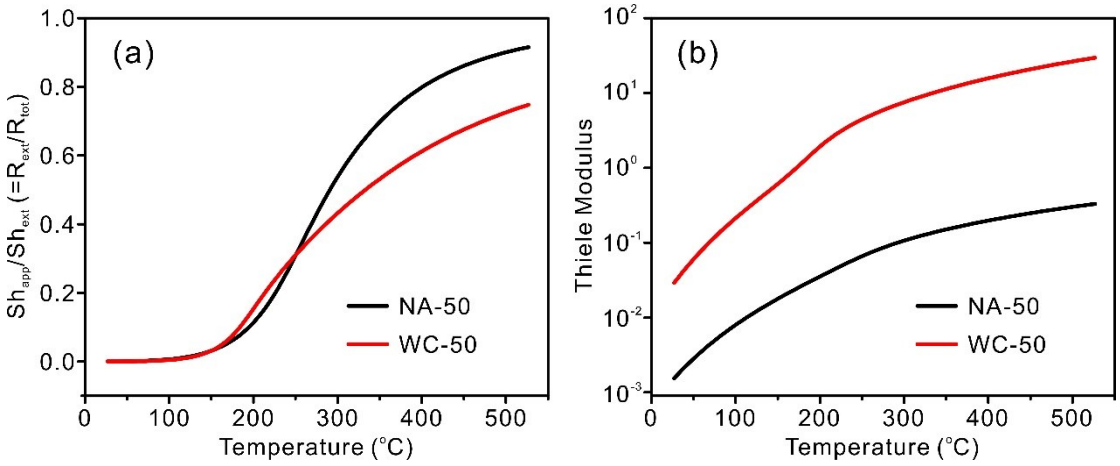

Figure 6. Calculated diagrams showing (a) the ratio of the experimentally observable Sherwood number to the actual external Sherwood number (Sh_{app}/Sh_e) and (b) the Thiele modulus as a function of the monolith temperature. Reaction gas feed conditions: C_{in} = 200 ppm C_2H_4, S.V. = 250,000/h.

The experimentally observable Sherwood number is always smaller than the theoretical asymptotic value. This indicates that the existence of kinetic resistance and internal mass transfer resistance at high temperature, and it is difficult to reach the pure external mass transfer controlled regime [59-61]. In this work, the ratio of the apparent Sherwood number Sh_{app} to the actual external Sherwood number Sh_e, Sh_{app}/Sh_e, equals the ratio of the external mass transfer resistance (R_{ex}) to the total resistance (R_{tot}) [57], and is dependent on the monolith temperature, as revealed in **Figure 6 (a)**. The experimentally observable Sh_{app} is always smaller than the external mass transfer coefficient (Sh_e), due to the existence of the kinetic resistance and internal mass transfer resistance. Since the reaction rate can be significant at high temperature, the kinetic resistance becomes negligible while the internal mass transfer resistance becomes dominant. As shown in **Figure 6 (a)**, the Sh_{app}/Sh_e of the NA-50

catalyst increases faster than the WC-50 catalysts, suggesting the external mass transfer resistance (R_{ex}) of the NA-50 catalyst approaches the total resistance (R_{tot}) faster than the WC-50 catalyst. In this case, the internal mass transfer resistance plays a negligible role in the nanoarray catalysts. The Thiele moduli of both catalysts along the monolith temperature are also plotted. The Thiele modulus is used to describe the relationship between diffusion and the reaction rate for the washcoat catalyst. In **Figure 6 (b)**, the Thiele modulus of the NA-50 catalyst is always smaller than that of the WC-50 catalysts over the entire temperature range. The smaller values of Thiele modulus over the nanoarray catalyst than the washcoat catalysts does not mean a lower reaction rate in the nanoarray catalysts, but indicates the fact that the effective diffusivity D_e in the nanoarray catalysts is much larger than that in the washcoat catalysts, as illustrated in **Eq. 12**.

To further compare the internal mass transfer resistance of the nanoarray and washcoat catalysts, the ratio of mass transfer coefficients, Sh_{app}/Sh_e of the NA-50 and WC-50 catalysts are plotted as a function of both the temperature and the position in the monolith channels in **Figure 7**. Two space velocities, 55,000/h and 250,000/h, were used to illustrate the difference between the NA-50 and WC-50 catalysts. As displayed in **Figure 7**, the experimental observable Sherwood number (Sh_{app}) of the NA-50 catalyst can reach 95% of the external Sherwood number (Sh_e) at ~600 °C **Figure 7(a)**. However, for the WC-50 catalyst, the ratio is smaller than 80% at this temperature **Figure 7(b)**. Clearly, the nanoarray catalysts have displayed much lower internal mass transfer resistance than the washcoat catalysts, as evidenced by the

faster kinetics at the intermediate temperature range. Meanwhile, comparing the profile of Sh_{app}/Sh_e of the NA-50 under different space velocities in **Figure 7(a)** and **Figure 7(c)**, no significant difference can be observed when the space velocity increases from 55,000/h to 250,000/h. However, for the washcoat catalysts WC-50, as shown in **Figure 7(b)** and **Figure 7(d)**, the temperature for the value of Sh_{app}/Sh_e to reach 80% increased from ~600 to ~700 °C when the velocity increases from 55,000/h to 250,000/h. This also shows that the internal mass transfer resistance does not play a significant role in the nanoarray-based monolithic catalysts.

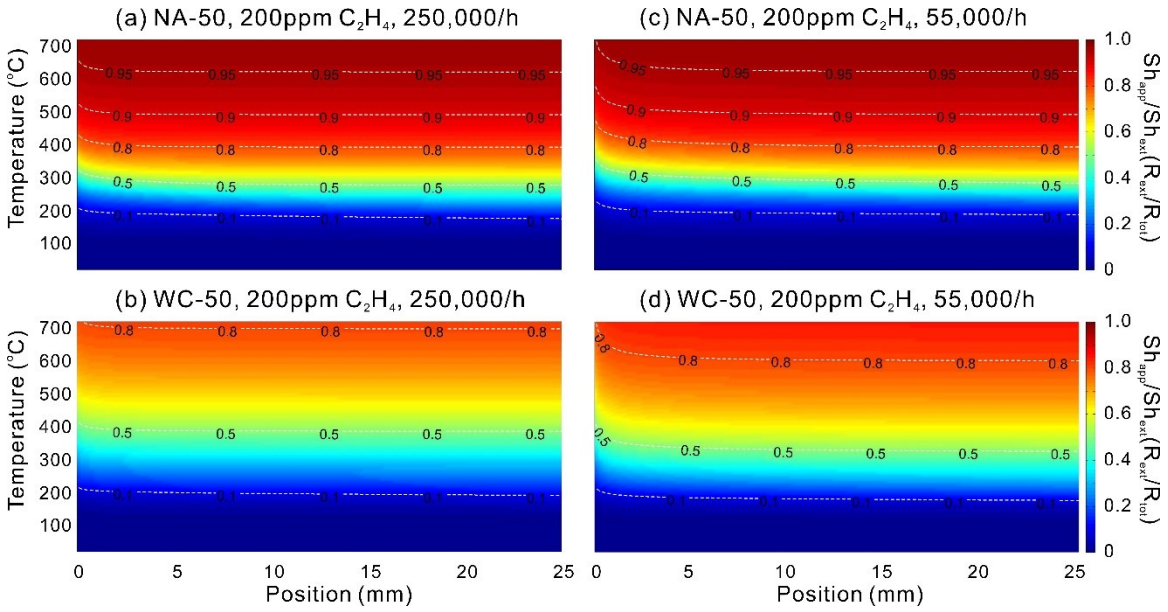

Figure 7. Model-predicted profiles of the ratio of the experimentally observable Sherwood number to the actual external Sherwood number, (Sh_{app}/Sh_e), along a monolithic channel and temperature on nanoarray and washcoat monolithic catalysts under different space velocities.

4.5. Internal Mass Transfer in Nanoarray Catalyst

Based on the above elaborated experimental and theoretical modelling results, nanoarray monolithic catalysts indeed showcase a significant advantage in lower internal mass transfer resistance than the washcoat counterparts. To derive this internal mass transfer resistance (R_{in}) quantitatively, **Eq. 14** can be used, i.e.:

$$R_{in} = \frac{1}{k_{mi}} = \frac{R_{\Omega_2}}{Sh_i D_e} \tag{14}$$

Clearly, the effective diffusivity (D_e) and the nanoarray/washcoat layer thickness (R_{Ω_2}) are two factors that determine R_{in}. Firstly, the nanoarray monoliths have high effective diffusivity due to the large volume of macropores. As well documented, the washcoat phase is a complex porous network which contains both mesopores (2~50nm) and macropores (>50nm). The mesopores can help to maximize the specific surface area while the macropores facilitate the overall mass transfer performance. Therefore, an increase in the percentage of macropores can help to increase the effective diffusivity [14, 62]. Researchers have been trying to increase the macroporous percentage by using sacrificing agents during the preparation of the washcoat [13]. However, an increase of macropores will compromise the mechanical and thermal stability of the washcoat catalysts. In the case of nanoarray configurations, the percentage of macropores can be simply estimated by calculating the volume ratio of the interspace between the nanoarray units. As shown in the SEM images of the nanoarrays in **Figure 1**, the nanoarrays are ~2 μm in length and ~50-100 nm in diameter. Meanwhile, the population density of the nanorods is ~96/μm^2, then the

volume ratio of nanorods is 48% in the nanoarray layer. If Knudsen diffusion is assumed within the nanorods and bulk diffusion in the interspace between the nanorods, the ratio of Knudsen diffusion volume can be 48%, while the ratio for bulk diffusion volume can be up to 52%. This means that the nanoarray layer is highly macroporous, which can greatly enhance the effective diffusivity of the reactant components within the nanoarray layer.

On the other hand, the internal mass transfer resistance can also be reduced by controlling the washcoat thickness (R_{Ω_2}), and that is another unique property of the nanoarray monolithic catalysts. As shown in **Figure 8**, the light-off curves of NA-50 and WC-50 in the case of gas feed conditions 1-3 (200 ppm C_2H_4, S.V. = 250,000/h) with different effective diffusivity coefficients ($D_f / D_e = \mu$) are plotted as a function of temperature. With the value of D_f / D_e increasing from 1 to 100, the light-off curves of the NA-50 catalysts do not change significantly, making the light-off curves almost overlapped with each other (**Figure 8a**). While for the WC-50 catalyst, the complete conversion temperatures are pushed to higher temperatures when the value of D_f / D_e increases (**Figure 8b**). The reason for the negligible influence of effective diffusivity on the performance of the NA-50 catalyst results from the small thickness of the nanoarray layer. Therefore, according to the **Eq. 14**, when the value of R_{Ω_2} is small, the internal mass transfer resistance can remain very small even with very low effective diffusivity (D_e).

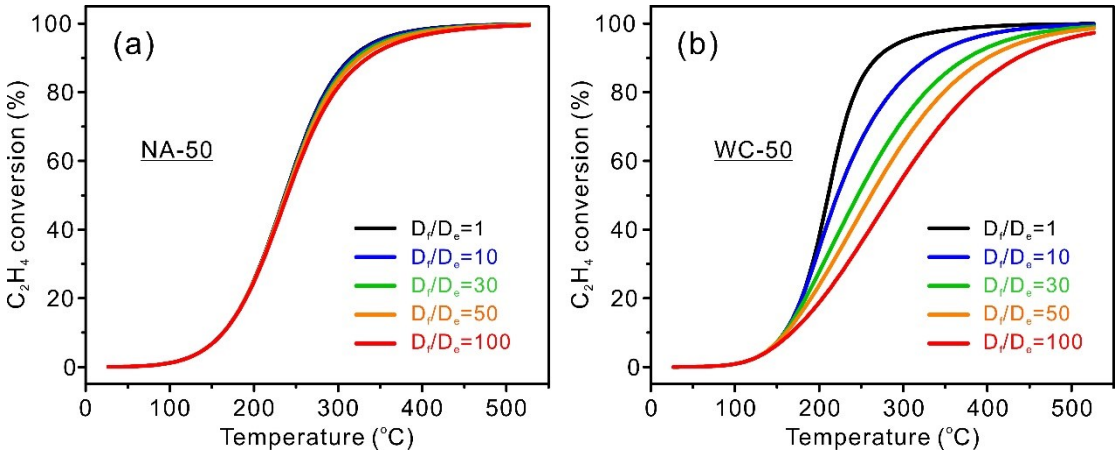

Figure 8. Influence of the effective diffusivity in the washcoat and nanoarray layers on the exit C_2H_4 conversion over the (a) NA-50 and (b) WC-50 catalysts. Reaction conditions: C_{in} = 200 ppm C_2H_4, S.V. = 250,000/h.

According to the above discussion on the thickness and effective diffusivity of the nanoarray and washcoat catalysts, the nanoarray can be viewed as a special type of washcoat with strong adhesion to monolithic substrates due to the in situ growth/manufacturing process. This special type of coatings is of well-ordered porosity, is ultrathin, highly macroporous, and mechanically stable. Meanwhile, it would be reasonable to predict that if the thickness of the classic washcoat layers is reduced to < 10 μm, their internal mass transfer efficiency would also be enhanced, as illustrated in **Figure S3**, which was also predicted in Joshi's work [9, 35]. Santos and Costa [14] also pointed out that the conversion efficiency of the monolithic catalysts can be improved by reducing the washcoat thickness and/or by increasing the effective diffusivity in the washcoat. However, when the classic washcoat thickness is reduced to several microns, its uniformity and mechanical stability throughout the monolithic device will be compromised due to the weak interfacial

adhesion between the traditional washcoat and substrate surfaces. Therefore, the classic washcoat layers have to be thick enough to provide sufficient support for the catalytic active materials. On the contrary, the *in situ* grown nanoarray-based monolithic catalysts as a novel catalytic configuration, however, could provide uniform and robust support materials with strong adhesion to the substrate for the catalytic active components while improving the internal mass transfer efficiency.

4.6. Performance of Nanoarray Monolithic Catalysts

Based on the discussion so far, the low internal mass transfer resistance results in a better performance of nanoarray catalysts than washcoat catalysts in the intermediate temperature range. The washcoat monolithic catalysts light off earlier than the nanoarray catalysts in the low-temperature range and the light-off curves of the nanoarray catalysts are slower to reach the conversion limits than the washcoat catalysts in the high temperature range when the space velocity is high (S.V. = 250,000/h), as shown in **Figure 2**. Therefore, it is necessary to provide strategies to improve the overall performance of the nanoarray-base monolithic catalysts over the entire temperature range.

Assuming a high space velocity condition, to improve the low temperature activity, specifically to lower the kinetic resistance, it is necessary to develop catalysts with high activity and/or high surface area. One of the potential strategies is to increase the specific surface area of the nanoarray layers. As shown in **Table 1**, the BET surface areas of the NA-50 and NA-10 catalysts are only half of those of the WC-50 and

WC-10 catalysts. This is due to the low loading of support materials in the nanoarray catalysts compared to the washcoat catalysts. The specific surface area of the nanoarray catalysts can be increased by either growing longer nanoarrays or using mesoporous materials with high specific surface area, such as zeolites. With higher specific surface area, the catalytic active components can be better dispersed, resulting an increased active surface area and improved low-temperature activity. On the other hand, the catalytic activity of catalysts also depends on other factors such as the valent states of the catalytic active components and the catalysts-support interaction. Therefore, the low-temperature conversion efficiency of the nanoarray catalysts can also be improved by employing more active catalysts, such as the bi-metallic catalysts such as Pt-Pd [39] and promoters like CeO_2 [21] and perovskite [26]. Furthermore, the catalytic activity can also be improved by optimizing the catalyst preparing procedure. For example, it was reported in our previous work that, by changing the loading method of Pt from dip-coating to wet-incipient impregnation, the dispersion of Pt catalysts on the TiO_2 nanoarrays can be increased from 24% to 74% with the same total loading amount of 50g/ft^3 [30].

Another strategy to improve the conversion efficiency of the monolithic catalysts is to develop a nanoarray/washcoat hybrid monolithic catalyst by combining the merits of the advanced nanoarray catalyst configuration and classical washcoat technology. On the one hand, nanostructured rough surface provided by array pre-grown substrate would enhance the anchoring/adhesion of washcoat particles, therefore thin washcoat layers can be stabilized on the monolith channel surfaces, keeping the internal mass

transport resistance low. On the other hand, the incorporated washcoats can increase the surface area of the nanoarray layers and make the catalytically active sites better dispersed. Therefore, the low-temperature conversion efficiency can be improved.

For the high-temperature conversion, according to **Eqs. 8** and **13**:

$$Sh_e = Sh_{H2,\infty} + \frac{0.108\left(f\,\mathrm{Re}\right)_{\infty}^{1/3}\left(\frac{P}{z}\right)}{1+0.083\left(\frac{P}{z}\right)^{2/3}} \tag{8}$$

$$R_{ex} = \frac{1}{k_{me}} = \frac{4R_{\Omega_1}}{Sh_e D_f} \tag{13}$$

The external mass transfer resistance R_{ex} depends on the hydraulic radius R_{Ω_1}, molecular diffusivity D_f and the external mass transfer coefficient Sh_e. R_{Ω_1} and D_f barely changed once the geometry of the monolith and reactant species are fixed. But the external Sherwood number Sh_e strongly depends on its asymptotic value, as Sh_e approaches $Sh_{\mathrm{H2},\infty}$ at high temperature. $Sh_{\mathrm{H2},\infty}$ depends on the geometric shape of the channels [63, 64]. As shown in **Table 1**, the values of $Sh_{\mathrm{H2},\infty}$ for the nanoarray monolith and washcoat monolith are 3.089 and 4.364 according to the channel shape shown in **Figure 1**, respectively [11]. Therefore, with the same R_{Ω_1} and D_f, the nanoarray monolithic catalysts have a higher external mass transfer resistance than the washcoat catalysts. In this case, the external mass transfer resistance of the nanoarray catalysts can be reduced by optimizing the design of the monolithic substrate. For example, the value of $Sh_{\mathrm{H2},\infty}$ of the hexagonal channels is 3.861, which is bigger than that of the square channel (3.089), and therefore a smaller external mass transfer

resistance existed at high temperature, as shown in **Figure 9 (a)**. On the other hand, the effect of $Sh_{H2,\infty}$ on the high-temperature conversion of the nanoarray catalysts only become significant at an extremely high space velocity such as 250,000/h shown in **Figure 9 (a)**. However, such high space velocity is not common in practical applications, and this problem can be spontaneously mitigated when the space velocity is low. For example, as indicated in **Figure 9 (b)**, when the space velocity is reduced to 55,000/h, a normal operation condition in automotive catalysts, the shape of the channel shape does not impose significant influence on the high-temperature conversion.

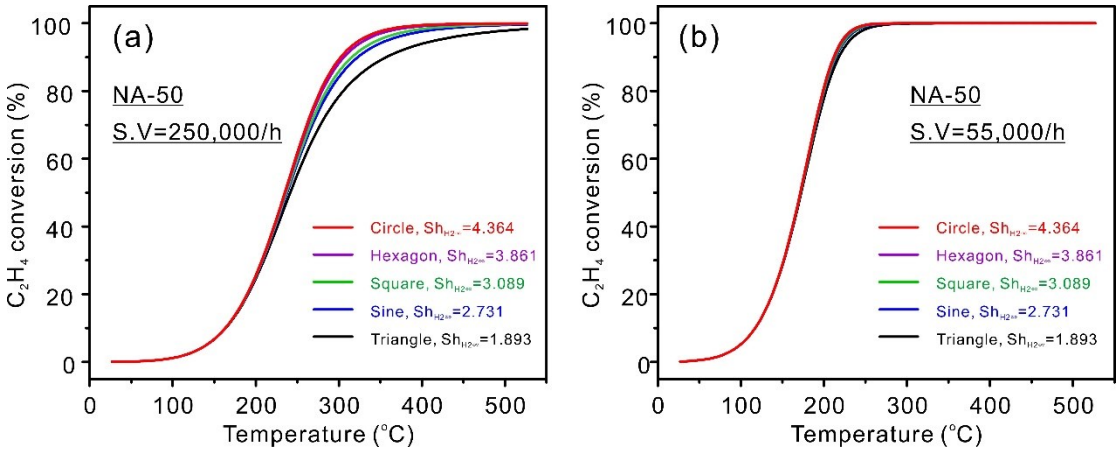

Figure 9. Influence of channel shape and space velocity on the exit C_2H_4 conversion over the NA-50 catalysts.

The modeling and related discussion in the present work are based on the experimental results of the NA-50 and WC-50 catalysts, as well as based on a gas feed assumption that may not favor practical catalyst operational conditions. However, the manifold results and analyses demonstrate that the low internal mass transfer resistance of the nanoarray catalysts is a universal phenomenon for catalytic gas phase

reactions. In fact, the nanoarray-based monolithic catalysts can be employed as an ideal catalyst configuration to study the catalytic reactions without the effects of internal mass transfer resistance. As for the further development of nanoarray catalysts, future efforts will be focused on the development of highly mesoporous and active nanoarray-based catalysts to increase the low-temperature activity as well as optimizing the geometries of monolith honeycombs to mitigate external mass transfer resistance under high space velocities. More practical operational conditions with multiple reactions, such as the simulated engine-out exhaust conditions, will also be employed to elucidate the mass transport properties of the nanoarray catalysts.

5. Conclusion

To summarize this work, firstly, by testing the catalytic performance towards C_2H_4 oxidation over a series of washcoat and nanoarray-based Pt/TiO_2 monolithic catalysts, we obtained direct experimental evidence for the lower internal mass transport resistance of the nanoarray monolithic catalysts than the washcoat catalysts. Second, we employed the low-dimensional model and quantified the contributions from the kinetic, internal mass transfer and external mass transfer resistance of the nanoarray and washcoat catalysts, which further showed lower internal mass transport resistance of the nanoarray catalysts than the washcoat catalysts in a theoretical way. Finally, we explained the low internal mass transfer resistance of the nanoarray catalysts by examining the effects of the effective diffusivity (D_e), nanoarray thickness (R_{Ω_2}), and the geometries of monoliths on the catalytic performance.

Ethylene is a fast-oxidizing hydrocarbon so the chemical reaction rate is highly temperature-sensitive around the light-off temperatures. We took this advantage to estimate the mass transport properties of both types of catalysts. C_2H_4 oxidation reactions were conducted on the Pt/TiO_2 nanoarray and washcoat monolithic catalysts under different feed concentrations of C_2H_4 and space velocities. The lower internal mass transfer resistance was directly observed by the steeper light off curves of the nanoarray catalysts than the washcoat counterparts at intermediate temperatures. The values of the apparent activation energy and reaction order numbers also demonstrated enhanced internal mass transfer efficiency of the nanoarray catalysts over their washcoat counterparts.

The low-dimensional model provides an efficient tool to study the mass transport properties of the monolithic catalysts. In this work, we employed the LD model and quantified the resistance contributions from the kinetic reactions, internal mass transfer and external mass transfer in the nanoarray (NA-50) and washcoat (WC-50) catalysts. The modeling results clearly showed that the internal mass transfer resistance of the nanoarray catalysts is an order of magnitude lower than the kinetic resistance and external mass transfer resistance, which is compared favorably with the significant internal mass transfer resistance of the washcoat catalysts.

The low internal mass transfer resistance of the nanoarray catalysts originates from the unique morphology and geometries of the nanoarray configuration. On the one hand, the abundant interspatial volume between the nanoarray units facilitate bulk diffusion, which results in a high effective diffusivity of the nanoarray catalysts. On

the other hand, the small thickness of the nanoarray layer further diminishes the internal mass transfer resistance during the catalytic reactions.

Being a robust and versatile catalyst platform, the nanoarray-based monolithic catalysts represent a model configuration which has negligible internal mass transfer resistance. This approach has the potential to partially substitute state-of-the-art washcoat catalysts in situations requiring low internal diffusion limitations. Future work on nanoarrays will be focused on developing highly active catalysts with high specific surface area, and optimizing the design of the substrate geometries. The rationale of the nanoarray/washcoat hybrid catalysts was also discussed. By combining the merits of the advanced nanoarray catalysts configuration and classical washcoat technology, it is possible to improve the low-temperature conversion efficiency and to reduce the internal mass transfer resistance of the monolithic catalysts at the same time. To sum up, the nanoarray configuration provides a new pathway toward designing high-performance monolithic catalysts with low internal diffusional limitations.

Nomenclature

η = exit conversion, %

C_f = averaged mole fraction of C_2H_4 in the fluid phase, mol/m^3

C_s = averaged mole fraction of C_2H_4 in the gas-solid interface, mol/m^3

$\langle C_{wc} \rangle$ = averaged mole fraction of C_2H_4 in the washcoat phase, mol/m^3

$\langle u \rangle$ = average fluid velocity, m/s

ε_{wc} = washcoat porosity

R_{Ω_1} = hydraulic radius (ratio of cross-section area to parameter), m

R_{Ω_2} = effective washcoat thickness, m

k_{me} = external mass-transfer coefficients, m/s

k_{me} = internal mass-transfer coefficients, m/s

D_f = temperature-dependent molecular diffusivity of reactant in the fluid phase, m^2/s

D_e = effective diffusivities in the washcoat phase, m^2/s

μ = ratio of D_f over D_e

Sh_e = external Sherwood number

Sh_i = internal Sherwood numbers

$Sh_{i,\infty}$ = asymptotic internal Sherwood numbers

$Sh_{H2,\infty}$ = asymptotic Sherwood number for fully developed flow

$(f\,\mathrm{Re})_\infty$ = friction factor times Reynolds number for fully developed flow

z = dimensionless length of monolith channel

P = transverse mass Peclet number

Λ = constant used in the universal correlation of r internal mass transfer coefficient

ϕ = Thiele modulus

TOR = reaction rate calculated per unit volume of washcoat, mol/m^3/s

R_{ex} = external mass transfer resistance, s/m

R_{in} = internal mass transfer resistance, s/m

R_{re} = kinetic reaction resistance, s/m

R_t = total resistance, s/m

k_{me} = external mass transfer coefficient, m/s

k_{mi} = internal mass transfer coefficient, m/s

k_{mapp} = apparent mass transfer coefficient, m/s

E_a = reaction activation energy, kJ/mol

Acknowledgements

The authors are grateful for the financial support from the US Department of Energy (Award Nos. DE-EE0006854, DE-SC0018890, and DE-EE0008423) and the US National Science Foundation (Award Nos. CBET1344792 and IIP-1919231). X.X. Lu is partially supported by a ThermoFisher Scientific Graduate Fellowship. The SEM and partial TEM studies were performed using the facilities in the UConn/ThermoFisher Scientific Center for Advanced Microscopy and Materials Analysis (CAMMA). The authors are grateful to Prof. Michael P. Harold, Ms. Zhiyu Zhou and Mingjie Tu for their insightful discussion on the low-dimensional model.

Declaration of Competing Interest

The authors declare that they have no known competing financial interests or personal relationships that could have appeared to influence the work reported in this paper.

References

[1] J.L. Williams, Monolith structures, materials, properties and uses, Catal. Today 69 (2001) 3-9.

[2] S. Du, W. Tang, X. Lu, S. Wang, Y. Guo, P.X. Gao, Cu-Decorated ZnO Nanorod Array Integrated Structured Catalysts for Low-Pressure CO_2 Hydrogenation to Methanol, Adv. Mater. Interfaces 5 (2018) 1700730.

[3] J.S. Choi, P. Kočí, Automotive Emission Control Catalysts, Multidisciplinary Digital Publishing Institute, Catalysts 6 (2016), 155.

[4] A.T. Bell, The Impact of Nanoscience on Heterogeneous Catalysis, Science 299 (2003) 1688-1691.

[5] A. Cybulski, J.A. Moulijn, Monoliths in Heterogeneous Catalysis, Catal. Rev. 36 (1994) 179-270.

[6] V. Tomašić, F. Jović, State-of-the-art in the monolithic catalysts/reactors, Appl. Catal., A 311 (2006) 112-121.

[7] H. Santos, M. Costa, The relative importance of external and internal transport phenomena in three way catalysts, Int. J. Heat Mass Transfer 51 (2008) 1409-1422.

[8] G.C. Koltsakis, A.M. Stamatelos, Catalytic automotive exhaust aftertreatment,

Prog. Energy Combust. Sci. 23 (1997) 1-39.

[9] S.Y. Joshi, M.P. Harold, V. Balakotaiah, Overall mass transfer coefficients and controlling regimes in catalytic monoliths, Chem. Eng. Sci. 65 (2010) 1729-1747.

[10] S.Y. Joshi, M.P. Harold, V. Balakotaiah, On the use of internal mass transfer coefficients in modeling of diffusion and reaction in catalytic monoliths, Chem. Eng. Sci. 64 (2009) 4976-4991.

[11] S.R. Gundlapally, V. Balakotaiah, Heat and mass transfer correlations and bifurcation analysis of catalytic monoliths with developing flows, Chem. Eng. Sci. 66 (2011) 1879-1892.

[12] S.Y. Joshi, Y. Ren, M.P. Harold, V. Balakotaiah, Determination of kinetics and controlling regimes for H_2 oxidation on Pt/Al_2O_3 monolithic catalyst using high space velocity experiments, Appl. Catal., B 102 (2011) 484-495.

[13] P.S. Dhillon, M.P. Harold, D. Wang, A. Kumar, S.Y. Joshi, Enhanced transport in washcoated monoliths: Application to selective lean NO_x reduction and ammonia oxidation, Chem. Eng. J. 377 (2019): 119734.

[14] H. Santos, M. Costa, Influence of the three way catalytic converter substrate cell density on the mass transfer and reaction resistances, Chem. Eng. Sci. 107 (2014) 181-191.

[15] Y. Guo, Z. Ren, W. Xiao, C. Liu, H. Sharma, H. Gao, A. Mhadeshwar, P.-X. Gao, Robust 3-D configurated metal oxide nano-array based monolithic catalysts with ultrahigh materials usage efficiency and catalytic performance tunability, Nano Energy 2 (2013) 873-881.

[16] Z. Ren, Y. Guo, P.-X. Gao, Nano-array based monolithic catalysts: Concept, rational materials design and tunable catalytic performance, Catal. Today 258 (2015) 441-453.

[17] J. Weng, X. Lu, P.-X. Gao, Nano-Array Integrated Structured Catalysts: A New Paradigm upon Conventional Wash-Coated Monolithic Catalysts?, Catalysts 7 (2017) 253.

[18] S. Wang, Y. Wu, R. Miao, M. Zhang, X. Lu, B. Zhang, A. Kinstler, Z. Ren, Y. Guo, T. Lu, Scalable continuous flow synthesis of ZnO nanorod arrays in 3-D ceramic honeycomb substrates for low-temperature desulfurization, CrystEngComm 19 (2017) 5128-5136.

[19] X. Lu, W. Tang, P.-X. Gao, Nanostructured TiO_2 Support Effect on Hydrothermal Stability of Platinum based Catalysts, Microsc. Microanal. 24 (2018) 1642-1643.

[20] Y. Fang, X. Chi, L. Li, J. Yang, S. Liu, X. Lu, W. Xiao, L. Wang, Z. Luo, W. Yang, S. Hu, J. Xiong, S. Hoang, H. Deng, F. Liu, L. Zhang, P. Gao, J. Ding, Y. Guo, Elucidating the Nature of the Cu(I) Active Site in CuO/TiO_2 for Excellent Low-Temperature CO Oxidation, ACS Appl. Mater. Interfaces 12 (2020) 7091-7101.

[21] W. Tang, X. Lu, F. Liu, S. Du, J. Weng, S. Hoang, S. Wang, C.-Y. Nam, P.-X. Gao, Ceria-based nanoflake arrays integrated on 3D cordierite honeycombs for efficient low-temperature diesel oxidation catalyst, Appl. Catal., B 245 (2019) 623-634.

[22] W. Tang, S. Wang, W. Xiao, S. Du, X. Lu, S. Hoang, J. Ding, P.-X. Gao, Pre-surface leached cordierite honeycombs for $MnxCo_{3-x}O_4$ nano-sheet array integration with enhanced hydrocarbons combustion, Catal. Today 320 (2019) 196-203.

[23] W. Tang, J. Weng, X. Lu, L. Wen, A. Suburamanian, C.-Y. Nam, P.-X. Gao, Alkali-metal poisoning effect of total CO and propane oxidation over Co_3O_4 nanocatalysts, Appl. Catal., B 256 (2019) 117859.

[24] Q. Shi, T. Liu, Q. Li, Y. Xin, X. Lu, W. Tang, Z. Zhang, P.-X. Gao, J.A. Anderson, Multiple strategies to decrease ignition temperature for soot combustion on ultrathin MnO_{2-x} nanosheet array, Appl. Catal., B 246 (2019) 312-321.

[25] J. Yang, W. Xiao, X. Chi, X. Lu, S. Hu, Z. Wu, W. Tang, Z. Ren, S. Wang, X. Yu, L. Zhang, A. Rusydi, J. Ding, Y. Guo, P.-X. Gao, Solar-driven efficient methane catalytic oxidation over epitaxial $ZnO/La_{0.8}Sr_{0.2}CoO_3$ heterojunctions, Appl. Catal., B (2019) 118469.

[26] W. Sibo, D. Shoucheng, T. Wenxiang, H. Son, L. Xingxu, X. Wen, Z. Bo, W. Junfei, S. Evan, G. Yanbing, D. Jun, Z. Zhaoliang, G. Pu-Xian, Mesoporous Perovskite Nanotube-Array Enhanced Metallic-State Platinum Dispersion for Low Temperature Propane Oxidation, ChemCatChem 10 (2018) 2184-2189.

[27] S. Du, S. Wang, Y. Guo, X. Lu, W. Tang, Y. Ding, X. Mao, P.-X. Gao, Rational design, synthesis and evaluation of ZnO nanorod array supported $Pt:La_{0.8}Sr_{0.2}MnO_3$ lean NO_x traps, Appl. Catal., B 236 (2018) 348-358.

[28] S. Wang, Z. Ren, Y. Guo, P.-X. Gao, Nano-array integrated monolithic devices:

toward rational materials design and multi-functional performance by scalable nanostructures assembly, CrystEngComm 18 (2016) 2980-2993.

[29] Z. Ren, Y. Guo, C.-H. Liu, P.-X. Gao, Hierarchically nanostructured materials for sustainable environmental applications, Front. Chem. 1 (2013) 18.

[30] S. Hoang, Y. Guo, A.J. Binder, W. Tang, S. Wang, J. Liu, H. Tran, X. Lu, Y. Wang, Y. Ding, E.A. Kyriakidou, J. Yang, T.J. Toops, T.R. Pauly, R. Ramprasad, P.-X. Gao, Activating low-temperature diesel oxidation by single-atom Pt on TiO_2 nanowire array, Nat. Commun. 11 (2020) 1062.

[31] Z. Ren, V. Botu, S. Wang, Y. Meng, W. Song, Y. Guo, R. Ramprasad, S.L. Suib, P.-X. Gao, Monolithically Integrated Spinel $M_xCo_{3-x}O_4$ (M=Co, Ni, Zn) Nanoarray Catalysts: Scalable Synthesis and Cation Manipulation for Tunable Low-Temperature CH_4 and CO Oxidation, Angew. Chem. Int. Ed. 53 (2014) 7223-7227.

[32] W. Tang, Z. Ren, X. Lu, S. Wang, Y. Guo, S. Hoang, S. Du, P.-X. Gao, Scalable Integration of Highly Uniform $Mn_xCo_{3-x}O_4$ Nanosheet Array onto Ceramic Monolithic Substrates for Low-Temperature Propane Oxidation, ChemCatChem 9 (2017) 4112-4119.

[33] U.S. DRIVE Advanced Combustion and Emission Control (ACEC) Tech Team. Low Temperature Aftertreatment (LTAT) Working Group. Aftertreatment Protocols for Catalyst Characterization and Performance Evaluation: Low Temperature Oxidation Catalyst Test Protocol, http://cleers.org/ltat-protocols (2015).

[34] X. Lu, S. Hoang, W. Tang, S. Du, S. Wang, F. Liu, W. Zhong, S.L. Suib, G. Yang, F.-Y. Zhang, P.-X. Gao, Direct Synthesis of Conformal Layered Protonated Titanate Nanoarray Coatings on Various Substrate Surfaces Boosted by Low-Temperature Microwave-Assisted Hydrothermal Synthesis, ACS Appl. Mater.

Interfaces 10 (2018) 35164-35174.

[35] S.Y. Joshi, M.P. Harold, V. Balakotaiah, Low-dimensional models for real time simulations of catalytic monoliths, AlChE J. 55 (2009) 1771-1783.

[36] S.Y. Joshi, Experimental and modeling studies for real time simulations of catalytic monolithic reactors, University of Houston, 2010.

[37] S. Hoang, X. Lu, W. Tang, S. Wang, S. Du, C.-Y. Nam, Y. Ding, R.D. Vinluan, J. Zheng, P.-X. Gao, High performance diesel oxidation catalysts using ultra-low Pt loading on titania nanowire array integrated cordierite honeycombs, Catal. Today 320 (2019) 2-10.

[38] X. Lu, W. Tang, S. Du, L. Wen, J. Weng, Y. Ding, W.S. Willis, S.L. Suib, P.-X. Gao, Ion-Exchange Loading Promoted Stability of Platinum Catalysts Supported on Layered Protonated Titanate-Derived Titania Nanoarrays, ACS Appl. Mater. Interfaces 11 (2019) 21515-21525.

[39] X. Auvray, L. Olsson, Stability and activity of Pd-, Pt- and Pd–Pt catalysts supported on alumina for NO oxidation, Appl. Catal., B 168-169 (2015) 342-352.

[40] L. Wen, R. Xu, C. Cui, W. Tang, Y. Mi, X. Lu, Z. Zeng, S.L. Suib, P.-X. Gao, Y. Lei, Template-Guided Programmable Janus Heteronanostructure Arrays for Efficient Plasmonic Photocatalysis, Nano Lett. 18 (2018) 4914-4921.

[41] M. Hu, L. Jin, X. Su, S. Bamonte, X. Lu, P. Gao, S.L. Suib, B. Liu, J. He, Polymer-Assisted Co-Assembly towards Synthesis of Mesoporous Titania Encapsulated Monodisperse PdAu for Highly Selective Hydrogenation of Phenylacetylene, ChemCatChem 12 (2020) 1476-1482.

[42] X. Lu, M. Li, S. Hoang, S.L. Suib, P.-X. Gao, Solvent effects on the heterogeneous growth of TiO_2 nanostructure arrays by solvothermal synthesis, Catal. Today in Press (2020).

[43] D. Bhatia, R.D. Clayton, M.P. Harold, V. Balakotaiah, A global kinetic model for NO_x storage and reduction on $Pt/BaO/Al_2O_3$ monolithic catalysts, Catal. Today

147 (2009) S250-S256.

[44] R. Raj, M.P. Harold, V. Balakotaiah, Steady-state and dynamic hysteresis effects during lean co-oxidation of CO and C_3H_6 over Pt/Al_2O_3 monolithic catalyst, Chem. Eng. J. 281 (2015) 322-333.

[45] B.E. Poling, J.M. Prausnitz, J.P. O'connell, The properties of gases and liquids, Mcgraw-hill New York 2001.

[46] S.Y. Joshi, A. Kumar, J. Luo, K. Kamasamudram, N.W. Currier, A. Yezerets, Combined experimental and kinetic modeling study of the bi-modal NO_x conversion profile on commercial Cu-SAPO-34 catalyst under standard SCR conditions, Appl. Catal., B 165 (2015) 27-35.

[47] P.S. Metkar, V. Balakotaiah, M.P. Harold, Experimental study of mass transfer limitations in Fe- and Cu-zeolite-based NH_3-SCR monolithic catalysts, Chem. Eng. Sci. 66 (2011) 5192-5203.

[48] L. Olsson, B. Andersson, Kinetic Modelling in Automotive Catalysis, Top. Catal. 28 (2004) 89-98.

[49] M. Li, S.A. Malamis, W. Epling, M.P. Harold, Steady state and lean-rich cycling study of a three-way NO_x storage catalyst: Modeling, Appl. Catal., B 242 (2019) 469-484.

[50] B.M. Shakya, M.P. Harold, V. Balakotaiah, Modeling and analysis of dual-layer NO_x storage and reduction and selective catalytic reduction monolithic catalyst, Chem. Eng. J. 237 (2014) 109-122.

[51] M. Tu, R. Ratnakar, V. Balakotaiah, Reduced Order Models with Local Property Dependent Transfer Coefficients for Real Time Simulations of Monolith Reactors, Chem. Eng. J. (2019) 123074.

[52] N. Tian, K. Xiao, Y. Zhang, X. Lu, L. Ye, P. Gao, T. Ma, H. Huang, Reactive sites rich porous tubular yolk-shell g-C_3N_4 via precursor recrystallization mediated microstructure engineering for photoreduction, Appl. Catal., B 253 (2019) 196-205.

[53] H.S. Fogler, Elements of Chemical Reaction Engineering, Prentice Hall PTR 2006.

[54] U. Ackelid, L. Olsson, L.G. Petersson, Ethylene Oxidation on Polycrystalline Platinum over Eight Orders of Magnitude in Ethylene Pressure: A Kinetic Study in the Viscous Pressure Regime, J. Catal. 161 (1996) 143-155.

[55] U. Ackelid, L.R. Wallenberg, L.G. Petersson, Kinetics of ethylene oxidation on plane Pt/SiO_2 catalysts in the viscous pressure regime: evidence of support activity, Catal. Lett 39 (1996) 129-139.

[56] J. Kua, W.A. Goddard, Chemisorption of Organics on Platinum. 2. Chemisorption of C_2H_x and CH_x on Pt(111), J. Phys. Chem. B 102 (1998) 9492-9500.

[57] S.Y. Joshi, Y. Ren, M.P. Harold, V. Balakotaiah, Experimental and Theoretical Investigation of Controlling Regimes during Lean Oxidation of Methane and Propylene on Pt/Al_2O_3 Monolithic Reactors, Ind. Eng. Chem 51 (2012) 7482-7492.

[58] H. Santos, M. Costa, On the quantification of the controlling regimes in automotive catalytic converters, AIChE J 57 (2011) 218-226.

[59] H. Santos, M. Costa, Analysis of the mass transfer controlled regime in automotive catalytic converters, Int. J. Heat Mass Transf. 51 (2008) 41-51.

[60] U. Ullah, S.P. Waldram, C.J. Bennett, T. Truex, Monolithic reactors: mass transfer measurements under reacting conditions, Chem. Eng. Sci. 47 (1992) 2413-2418.

[61] J. Votruba, O. Mikuš, K. Nguen, V. Hlaváček, J. Skřivánek, Heat and mass transfer in honeycomb catalysts—II, Chem. Eng. Sci. 30 (1975) 201-206.

[62] P.S. Dhillon, M.P. Harold, D. Wang, A. Kumar, S. Joshi, Hydrothermal aging of Pt/Al_2O_3 monolith: Washcoat morphology degradation effects studied using ammonia and propylene oxidation, Catal. Today 320 (2019) 20-29.

[63] D.H. West, V. Balakotaiah, Z. Jovanovic, Experimental and theoretical

investigation of the mass transfer controlled regime in catalytic monoliths, Catal. Today 88 (2003) 3-16.

[64] V. Balakotaiah, D.H. West, Shape normalization and analysis of the mass transfer controlled regime in catalytic monoliths, Chem. Eng. Sci. 57 (2002) 1269-1286.